energies

MDPI

*Article*

# Temperature-Sensitive Paints and Thermochromic Liquid Crystals—A Direct Comparison for Heat Transfer Measurements †

**Marvin Tigre Larschow *, Paul David Hägele, Kai Michalek and Rico Poser**

Institute of Aerospace Thermodynamics, Faculty of Aerospace Engineering and Geodesy, University of Stuttgart, 70569 Stuttgart, Germany; paul-david.haegele@itlr.uni-stuttgart.de (P.D.H.); rico.poser@itlr.uni-stuttgart.de (R.P.)

* Correspondence: marvin-tigre.larschow@itlr.uni-stuttgart.de

† This paper is an extended version of our published extended abstract, available under ISSN 2562-9034 and indexed in Scopus.

**Abstract**

The number of suitable techniques for spatially resolved measurements of wall temperatures in internal flows is limited. Thermography using thermochromic liquid crystals (TLCs) is an established method that relies on a surface colour change to measure temperatures within a narrow band. Temperature-sensitive paints (TSP), by contrast, provide continuous temperature distributions over a wider temperature range through temperature-dependent luminescence intensity. While TLCs exhibit a lower absolute measurement uncertainty within their calibrated temperature range, TSPs allow the surface temperature to be measured continuously throughout the test period. In this work, a single-layer TLC configuration (sTLC), a multilayer TLC configuration (mTLC), and TSP are applied in three ribbed subchannels, enabling a direct technique-specific comparison under equal conditions and simultaneous evaluation. The time-dependent surface temperatures are evaluated using a transient semi-infinite wall (SIW) approach adapted to each technique. For the investigated range, the geometric mean heat transfer coefficient (HTC) differs by approximately 4% between sTLC and mTLC and by approximately 13% between sTLC and TSP. Larger local deviations are confined to the immediate vicinity of the high-gradient flank, where TSP yields a lower peak HTC and a higher HTC on the adjacent lower-gradient side than the TLC reference. Lateral heat conduction within the substrate is discussed as a possible cause. The measured temporal surface-temperature evolution was also compared with the analytical model. Good agreement is obtained in regions with high HTC, whereas a temperature plateau is observed in the TSP measurements in regions with low HTC. Finally, Monte Carlo simulations are demonstrated to estimate the measurement uncertainty of all evaluated techniques.

**Keywords:** temperature sensitive paint; liquid crystal thermography; wall temperature measurement; internal flow; ribbed channel; optical measurement

Check for updates

Academic Editor: Mahmoud Bourouis

Received: 24 August 2026
Revised: 23 September 2026
Accepted: 4 October 2026
Published: 9 October 2026

**Copyright:** © 2026 by the authors. Licensee MDPI, Basel, Switzerland. This article is an open access article distributed under the terms and conditions of the Creative Commons Attribution (CC BY) license.

## 1. Introduction

Efficient thermal design of thermally stressed components involves cooling mechanisms that serve different purposes in terms of installation space and heat dissipation. Their optimal use requires knowledge of heat conduction within the component as well as

convective heat transfer at solid–fluid interfaces. The convective performance is described by the heat transfer coefficient $h$ (HTC), defined as

$$h = \frac{\dot{q}_w}{T_w - T_{ref}} \quad (1)$$

where $T_w$ is the wall surface temperature, $T_{ref}$ is the fluid reference temperature, and $\dot{q}_w$ is the wall surface heat flux. Non-intrusive, spatially resolved techniques are particularly suitable for measuring wall temperatures over time and space, even in complex geometries. Thermochromic liquid crystals (TLC) and infrared thermography (IRT) are commonly used for this purpose [1,2].

TLCs indicate a calibrated temperature precisely and reliably, whereas IRT can measure a wide temperature range. While the measurement area must be optically accessible for TLC applications, the access paths to the measurement area must be infrared-transmissive for IRT. A direct comparison of the two techniques was conducted, for example, by Piasecka et al., using flow boiling heat transfer in a minichannel as a case study. In that case, the mean relative HTC differences between both techniques remained below 15 % [3].

Several studies have also applied temperature-sensitive paints (TSP) to determine surface temperatures and to derive heat transfer distributions from them [4–6]. Similar to IRT, TSP can resolve a wide temperature range. Unlike IRT, however, this information is obtained in the visible spectrum, so that the surface can also be observed through glass or PMMA, which are opaque in the infrared [5]. Al Hashimi et al. took advantage of precisely this benefit of TSP over IRT to measure time-resolved temperature and heat transfer distributions directly at the interface between the wall and the fluid during boiling processes [7]. Lorenz et al. conducted a direct comparison between TSP and IRT. Within the measurement area, the two techniques showed a root-mean-square deviation of 1.2 K relative to each other, and the maximum deviation from thermocouple readings was 0.5 K [8].

For internal flows observed through transparent PMMA walls, IRT cannot access the surface, and TLC and TSP are the relevant optical techniques. Despite the use of TLC and TSP to determine heat transfer, a quantitative comparison under identical experimental conditions is, to the authors' knowledge, still lacking. In this work, the techniques are compared within the same experiment in terms of their spatial HTC distributions and geometric mean values, their temporal surface-temperature evolution, and their measurement uncertainty.

## 2. Semi-Infinite Wall Method (SIW)

*Analytical Background*

The evaluation of the convective heat transfer is based on the transient semi-infinite wall approach. An initially isothermal wall is exposed to a sudden change of the fluid temperature, and the transient response of the wall temperature is recorded. Since this response is uniquely linked to the heat flux entering the wall, the HTC can be inferred from a measured pair of wall temperature and corresponding indication time, provided that the thermal properties of the wall material and the fluid temperature history are known. Neither a steady state nor a direct measurement of the wall heat flux is required, and, as the evaluation is performed locally, spatially resolved HTC distributions are obtained.

For the analysis, heat conduction within the wall is modelled as one-dimensional, with homogeneous and temperature-independent material properties, and the wall is assumed

to be semi-infinite in the direction normal to the surface. In the absence of internal heat sources or sinks, Fourier's law yields

$$\frac{\partial T}{\partial t} = a\,\frac{\partial^2 T}{\partial x^2}, \qquad a = \frac{k}{\rho c}, \tag{2}$$

subject to the initial condition $T(x, t = 0\,\mathrm{s}) = T_0$, the far-field condition $T(x \to \infty, t) = T_0$, and a convective boundary condition at the surface exposed to the flow at $x = 0\,\mathrm{m}$,

$$-k\,\frac{\partial T}{\partial x}\bigg|_{x=0} = h\,\big(T_\mathrm{F}(t) - T_\mathrm{w}(t)\big). \tag{3}$$

The far-field condition holds as long as the thermal penetration depth remains small compared with the wall thickness, which limits the admissible observation time. The corresponding requirement was verified in advance using the relation presented by Vogel and Weigand [9],

$$L > \sqrt{\frac{t\,a}{0.35}}, \tag{4}$$

where $L$ denotes the minimum wall thickness required for an observation time $t$ before the thermal penetration reaches the external wall side. With $a = 0.11 \times 10^{-6}\,\mathrm{m^2\,s^{-1}}$ and a channel wall thickness of $\delta_\mathrm{PMMA} = 28\,\mathrm{mm}$, an admissible test duration of $t_\mathrm{max} = 2494\,\mathrm{s}$ results, which exceeds the duration of all experiments reported here (maximum test duration is 120 s).

For an ideal temperature step from $T_0$ to $T_\mathrm{F}$ at $t = 0\,\mathrm{s}$ and a time-invariant HTC, the surface temperature response follows from the closed-form solution given by Carslaw and Jaeger [10] as

$$\frac{T_\mathrm{w}(t) - T_0}{T_\mathrm{F} - T_0} = 1 - \exp\left(\beta^2\right)\mathrm{erfc}(\beta), \qquad \beta = \frac{h\sqrt{at}}{k}, \tag{5}$$

where erfc denotes the complementary error function.

In an experiment, an ideal temperature step is difficult to realise. On the one hand, the heater exhibits a finite thermal inertia, so that the fluid temperature rises over a finite period of time rather than instantaneously. On the other hand, and more relevant for the present configuration, the fluid temperature decreases progressively in the streamwise direction as heat is exchanged with the wall. The local driving temperature history is therefore not only delayed but also attenuated with respect to an ideal step, which leads to a systematic shift of the response curve if it is neglected [11]. Consequently, the measured time-dependent fluid temperature $T_\mathrm{F}(\tau)$ is accounted for by means of Duhamel's superposition principle [12], in which the actual fluid temperature history is decomposed into a sequence of elementary steps whose individual responses are superimposed. In the present work, the superposition is implemented in the discrete, noise-resistant reformulation of Hägele and Poser [13], where the differentiation is transferred from the measured fluid temperature signal to the analytical step response function, thereby reducing the sensitivity of the evaluation to measurement noise. In addition, the distance $z$ between the surface exposed to the flow and the temperature-indicating layer is taken into account, since it constitutes a significant parameter for the determination of the HTC [14].

With these considerations, the response of the wall at the depth $z$ to an ideal step of the fluid temperature is described by the step response function

$$\Theta(t) = \mathrm{erfc}\left(\frac{z}{2\sqrt{a\,t}}\right) - \exp\left(\frac{h\,z}{k} + \frac{h^2 a\,t}{k^2}\right)\mathrm{erfc}\left(\frac{z}{2\sqrt{a\,t}} + \frac{h\sqrt{a\,t}}{k}\right), \tag{6}$$

which reduces to Equation (5) for $z = 0\,\mathrm{m}$. Superimposing the discretely sampled fluid temperature history according to [13] finally yields the governing equation of the evaluation,

$$T_{\mathrm{ind}} - T_0 = -T_0\,\Theta(t_{\mathrm{ind}}) - \sum_{i=0}^{N-1} \frac{T_{\mathrm{F},i} + T_{\mathrm{F},i+1}}{2} \times \left[\Theta(t_{\mathrm{ind}} - \tau_{i+1}) - \Theta(t_{\mathrm{ind}} - \tau_i)\right], \tag{7}$$

where $T_{\mathrm{ind}}$ denotes the wall temperature indicated at the indication time $t_{\mathrm{ind}}$, and $T_{\mathrm{F},i} = T_{\mathrm{F}}(\tau_i)$ the fluid temperature at the discrete sampling instants $\tau_i$ with $\tau_0 = 0\,\mathrm{s}$ and $\tau_N = t_{\mathrm{ind}}$. Since $h$ appears implicitly within the step response function, Equation (7) cannot be inverted analytically and is solved numerically for each pixel.

Using the analysis method presented here, the HTC can be determined on a pixel-by-pixel basis, provided that, in addition to the constant material properties $(\rho, c, k)$, the initial temperature $T_0$, and the recorded fluid temperature history $T_{\mathrm{F}}(\tau)$, at least one wall temperature has been measured together with the corresponding indication time. For a single such pair, Equation (7) constitutes a determined problem and yields exactly one value of $h$. If, however, the measurement technique provides $M > 1$ temperature–time pairs $(T_{\mathrm{ind},j},\, t_{\mathrm{ind},j})$ for the same pixel, the problem becomes over-determined. In this case, Equation (7) is rearranged into residual form,

$$r_j(h) = T_0 - T_{\mathrm{ind},j} - T_0\,\Theta(t_{\mathrm{ind},j}) - \sum_{i=0}^{N_j-1} \frac{T_{\mathrm{F},i} + T_{\mathrm{F},i+1}}{2} \Big[\Theta(t_{\mathrm{ind},j} - \tau_{i+1}) - \Theta(t_{\mathrm{ind},j} - \tau_i)\Big], \tag{8}$$

so that one residual is obtained per pair, each vanishing for the HTC that reproduces the respective observation exactly. Rather than evaluating the pairs individually, the residuals are combined into a single objective function, and the HTC of the pixel is determined as the value that minimises all of them simultaneously,

$$h = \arg\min_{h} \sum_{j=1}^{M} w_j\, r_j^2(h). \tag{9}$$

The weights $w_j$ rate the individual pairs according to the precision with which the HTC can be inferred from each of them alone at the respective pixel. They follow by inverse-variance weighting, $w_j = u_j^{-2}$, from an estimate $u_j$ of the corresponding standard uncertainty. Since this estimate depends on the measurement technique and on the quantities entering the respective evaluation, its determination is addressed separately in Section 4.2. For $M = 1$ the sum contains a single term, the weight cancels, and Equation (9) reduces to the root of Equation (8), so that the determined case is recovered as a special case of the formulation above.

## 3. Experimental Setup

*Ribbed Channel Geometry*

To directly compare the measurement techniques, the experimental setup shown in Figure 1a is used. The central element is a flat PMMA (poly(methyl methacrylate)) channel subdivided into five equal subchannels. Table 1 summarizes the experimental boundary conditions.

As shown in Figure 1b, the three middle subchannels are used for the comparison. Subchannels 1 and 5 are excluded from the analysis because of edge effects. Subchannel 2 is equipped with TSP, subchannel 3 with the single TLC (sTLC) configuration, and

subchannel 4 with the multilayer TLC (mTLC) configuration. The flow length of each subchannel is 812.5 mm. All subchannels have an equal upper-wall geometry (Figure 1c) and are equipped with 13 diagonally oriented ribs. The dimensionless parameters are $P/e = 10$ and $e/d_h = 1.75$. In front of and behind the ribbed section, there is an unribbed inlet and outlet section of 10.5 $d_h$. The entire channel is operated in suction mode with a heated air flow. Previous work has already ensured that both the mass flow rate of air and the heat transfer processes are equal within the measurement uncertainty between subchannels 2 through 4 (maximum deviation in mass flow between channels is 0.04%) [15].

**Table 1.** Operating conditions of the heat transfer experiment. Mass flow is referenced to dry air.

| Quantity | Symbol | Value |
|---|---|---|
| Total mass flow rate | $\dot{m}$ | $0.57\,\mathrm{kg\,s^{-1}}$ |
| Temperature step | $\Delta T_{\mathrm{step}}$ | 36 K |

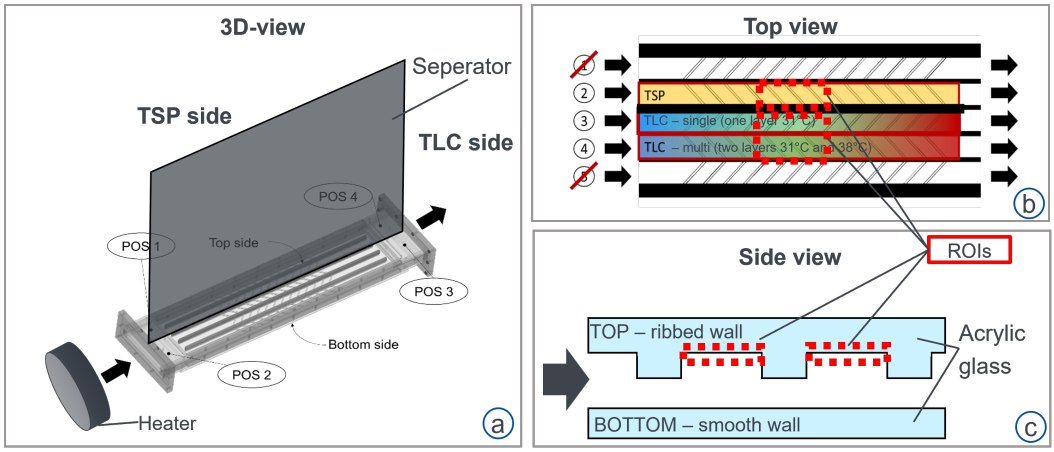



**Figure 1.** Experimental design of the ribbed-channel test section and optical measurement setup: (**a**) three-dimensional overview; (**b**) top view showing the TSP subchannel (2), sTLC subchannel (3), and mTLC subchannel (4); (**c**) side view of an example subchannel with the labelled regions of interest (ROIs).

The two measurement techniques used to determine the surface temperatures in the ribbed area are based on different and partly conflicting optical requirements. The TLC is illuminated with full-spectrum light and recorded using colour cameras, whereas the TSP area is darkened and recorded using a monochrome camera with an optical filter. The UV radiation used to excite the TSP also accelerates TLC ageing and must therefore be prevented from reaching the TLC side. The two optical systems are consequently separated physically. Their cameras also differ in pixel size and sensor resolution. To maximise comparability, the lenses and camera positions were selected such that both systems resolve an ROI, extending across three fully resolved ribs in the centre of the channel, at the same spatial resolution (Figure 1b).

## 4. Measurement Principles

### *4.1. Thermochromic Liquid Crystals*

TLCs are chiral nematic compounds whose molecules arrange in a helical structure, the pitch of which decreases reversibly with increasing temperature [16]. Incident white light is selectively reflected at this periodic structure by Bragg reflection, so that the reflected wavelength scales with the local pitch and the coating traverses the visible spectrum from red to blue as the temperature rises [1]. Outside this activation range the material

remains essentially transparent; a light-absorbing background is therefore required to suppress the transmitted light and to provide the contrast needed for reliable detection of the colour play. In the present work, narrowband formulations with a nominal bandwidth of 1 K are employed (LCR Hallcrest R31C1W and R38C1W, hereafter denoted by $TLC_{31}$ and $TLC_{38}$). The colour play is therefore confined to a narrow temperature interval, and one sharply defined indication temperature can be assigned to each layer. Two coating configurations are used throughout this work: the single-layer TLC configuration (sTLC) contains only $TLC_{31}$ and yields one temperature–time pair per pixel, whereas the multilayer TLC configuration (mTLC) combines $TLC_{31}$ and $TLC_{38}$ in a stack and provides two pairs with different indication temperatures and times for the same pixel.

#### 4.1.1. TLC Setup

The layer arrangement of both configurations is shown in Figure 2. The coatings are sprayed onto the inner surface of the transparent channel wall and are observed from the outside through the wall, with the black background applied last so that it forms the surface exposed to the flow. Since each indicating layer is thus located at a finite distance behind that surface, the evaluation depth $z$, defined as the distance from the surface exposed to the flow to the mid-plane of the respective layer, has to be accounted for in the evaluation, as it constitutes a significant parameter for the determination of the HTC [14]. The thickness of every individual layer was determined by profilometry on a special test specimen that replicated the model's spray sequence, from which the evaluation depths follow as the cumulative thickness of the preceding layers plus half the thickness of the layer itself. After drying, the layer thickness on the specified test specimen was measured using a calibrated Elcometer A456CNSS with an accuracy of 2.5 µm. To determine the respective thickness, 20 measurements were taken in each case, and the mean value and standard deviation were calculated. The resulting values are summarised in Table 2. Because $TLC_{38}$ is located beneath $TLC_{31}$, the evaluation depth of $TLC_{31}$ is equal for both configurations. The total coating thickness is deliberately not minimized, since for TLC, the optimal coating thickness should be between 10 µm and 20 µm [17]. While a smaller evaluation depth reduces the thermal lag between the surface exposed to the flow and the indicating layer, excessively thin coatings reflect markedly less light and thus produce a weaker and less distinct colour play, so that the thickness represents a compromise between both effects.

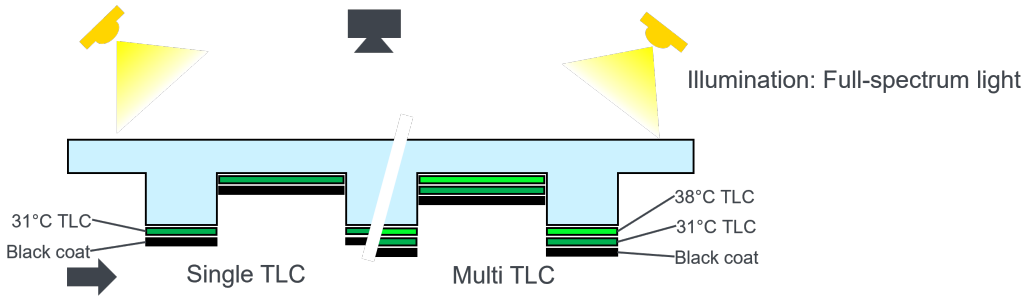



**Figure 2.** Schematic of the optical setup and layer arrangement for the sTLC and mTLC configurations. The arrow indicates the flow direction and the side exposed to the flow.

**Table 2.** Layer thicknesses $\delta$ measured using a Elcometer A456CNSS, evaluation depths $z$ and calibrated indication temperatures $T_{ind}$ of the coating stack, listed in the order of increasing distance from the surface exposed to the flow.

| Layer | $\delta$/µm | $z$/µm | $T_{ind}$/°C |
|---|---|---|---|
| Black background | 8.55 | – | – |
| $TLC_{31}$ | $9.01 \pm 2.74$ | 13.06 | $31.399^{+0.091}_{-0.095}$ |
| $TLC_{38}$ | $10.66 \pm 2.89$ | 22.89 | $40.266^{+0.157}_{-0.110}$ |

#### 4.1.2. TLC Calibration

Because the reflected wavelength depends not only on temperature but also on coating composition and illumination, every layer is calibrated individually. The calibration is performed in a separate steady-state procedure before the experiments, following Poser and von Wolfersdorf [18]. The coated surface is successively brought to steady temperature levels measured by thermocouples in the immediate vicinity of the observed area. An image is recorded after thermal equilibrium has been established. The illumination, camera settings, and optical arrangement are identical to those used in the subsequent experiments. The recorded image is decomposed into its red, green, and blue channels, and the indication temperature of a layer is defined as the temperature at which the green intensity reaches its maximum ($G_{max}$). The green channel is preferred because it carries the highest information density of the three: its intensity histories deviate most strongly from a purely random signal, and its maximum is narrow and pronounced rather than broad, so that it can be localised substantially more sharply than the maxima of the red and blue channels [19]. The indication temperatures obtained in this way are listed in Table 2. To minimise differences in illumination between the experiment and the calibration, the same lamps, camera and optical arrangement are used in both cases, so that the illumination and viewing angles are identical for every pixel. Since the perceived colour of a TLC coating depends on both angles [20], this ensures that any such dependence affects calibration and experiment in the same way and is thus contained in the calibrated indication temperature. In addition, the indication criterion is based on the temporal position of the green-intensity maximum rather than on absolute intensity levels, so that spatially non-uniform illumination alters the level of the recorded histories but not the detected instant.

#### 4.1.3. TLC Post-Processing

During the experiments, the coated surface is recorded as an image sequence, from which the green-channel intensity history is extracted for every pixel. Applying the same criterion as in the calibration, the indication time $t_{ind}$ is identified as the instant at which this history reaches its maximum, so that each pixel yields one temperature–time pair per indicating layer. These maxima are not detected directly from the raw histories because the signal of an individual pixel contains noise and, in the mTLC configuration, the two layers indicate at different times and must be separated. Both tasks are performed using the image-processing routine presented in [21], which was developed specifically for transient experiments with stacked TLC layers.

Beyond the indication times themselves, this routine also quantifies how distinctly each indication is resolved at the respective pixel and returns a confidence interval around $t_{ind}$. Its width is a direct measure of the local signal quality: sharply pronounced maxima yield narrow intervals, whereas flat or noise-dominated histories yield broad ones. This information is retained on a pixel-by-pixel basis and enters the subsequent evaluation as the uncertainty of the indication time and, for the mTLC configuration, as the weighting between the two layers, as described in the following section.

### *4.2. Quality Rating of the TLC Indications*

The weighting in Equation (9) requires an estimate $u_j$ of the standard uncertainty associated with each temperature–time pair. For the TLC measurements, in which each layer contributes one calibrated activation temperature $T_{ind,j}$ at its detected indication time $t_{ind,j}$, this estimate is obtained from the equivalent ideal-step uncertainty analysis according to Poser and von Wolfersdorf [18]. The underlying idea is to assign to each pair the ideal temperature step that would reproduce the same HTC at the same indication time, so that the closed-form solution can be inverted analytically and the sensitivity

coefficients with respect to the material properties, the involved temperatures, and the indication time become accessible without a numerical propagation through the complete model. The uncertainty of the indication time itself is taken from the signal analysis of the respective pixel; indications whose relative interval width exceeds 20 % are rejected individually rather than for the pixel as a whole, so that a poorly detected indication of one layer does not discard the information of the other. Since these sensitivity coefficients depend on $h$, which in turn depends on the weights, the weighting and the minimisation are solved jointly in a fixed-point iteration. Starting from uniform weights, the iteration is terminated once the largest change of any weight between two successive iterations falls below $10^{-3}$; as the weights are normalised to $\sum_j w_j = 1$, this is an absolute criterion on a bounded quantity. The update map is a contraction with a modulus below $3.1 \times 10^{-3}$ throughout the evaluated field, so that by Banach's fixed-point theorem [22,23] the fixed point is unique and the criterion is met after two iterations at every pixel. After evaluating Equation (9), the resulting $h$ is used to update all $u_j$, and the procedure is repeated until the weights become stationary. The resulting rating is governed by two opposing effects. For indications occurring within the first seconds of the transient, the uncertainties of the time measurement dominate. Both the detection of the indication instant and the synchronisation of the camera and thermocouple time bases contribute here, and since the wall temperature still changes rapidly at this stage, a small temporal offset already corresponds to a pronounced change in HTC. For late indications, in contrast, the difference between fluid and wall temperature approaches its asymptotic value and thus changes only slowly. Small errors in the temperature measurements therefore translate into a considerable deviation in HTC, which applies both to the thermocouple readings of the fluid temperature and to the calibration of the TLC indication temperature. Indications recorded in the intermediate regime are consequently rated highest, while those acquired close to either end of the transient contribute less to the combined result.

### *4.3. Temperature-Sensitive Paints*

#### 4.3.1. TSP Setup

For TSP thermography, the luminophore Europium(III) thenoyltrifluoroacetonate trihydrate ($Eu(TTA)_3 \cdot 3\,H_2O$, CAS 21392-96-1, 95 % purity) is excited by high-energy UV light at 365 nm and emits Stokes-shifted light at approximately 612 nm. The luminophores are embedded in a clear coat that forms the temperature-sensitive layer and is sprayed directly onto the inner surface of the PMMA channel. A white background reflects both the excitation light and the emitted luminescence, while a black top coat faces the flow and provides the same surface roughness as in the TLC subchannels. Two external UV LEDs illuminate the coating through the UV-transparent PMMA test specimen, ensuring effective external excitation. A centrally mounted monochrome camera records the emission through a long-pass filter ($\lambda > 550$ nm), which suppresses the excitation light and prevents non-luminescent radiation from reaching the sensor [24] (see Figure 3).

The specified layer thicknesses for the TSP setup are listed in Table 3. The measurement procedure is identical to that for TLC described in Section 4.1.1.

**Table 3.** Layer thicknesses $\delta$ measured using a Elcometer A456CNSS and the evaluation depths $z$ of the coating stack of the TSP, listed in the order of increasing distance from the surface exposed to the flow.

| Layer | $\delta$/µm | $z$/µm |
|---|---|---|
| Black background | 8.55 | – |
| White coat | $69.1 \pm 3.50$ | – |
| TSP coat | $2.54 \pm 1.39$ | 78.92 |

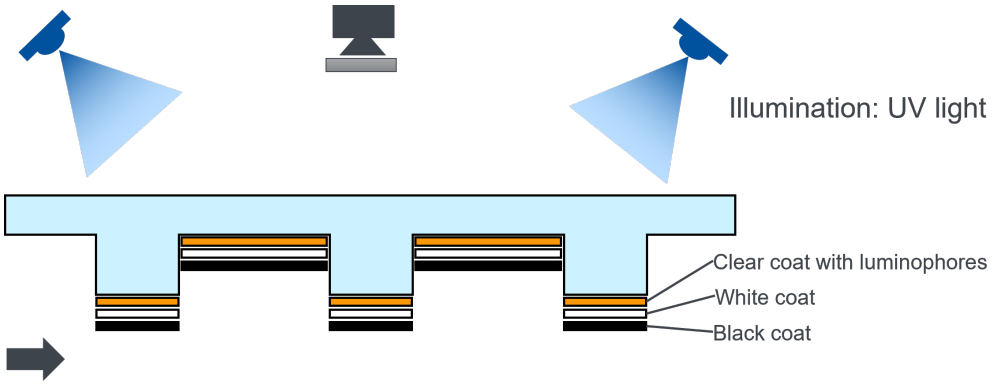



**Figure 3.** Schematic illustration of the setup on TSP side. The arrow indicates the flow direction and the side exposed to the flow.

#### 4.3.2. TSP Calibration

To correlate the TSP emission with a specific temperature, the paint was first calibrated in a separate setup. During the coating of the main sample, a smaller acrylic-glass sample with the same layer structure and composition was also coated. In the calibration setup (Figure 4), this sample was mounted on a temperature PID-controlled surface.

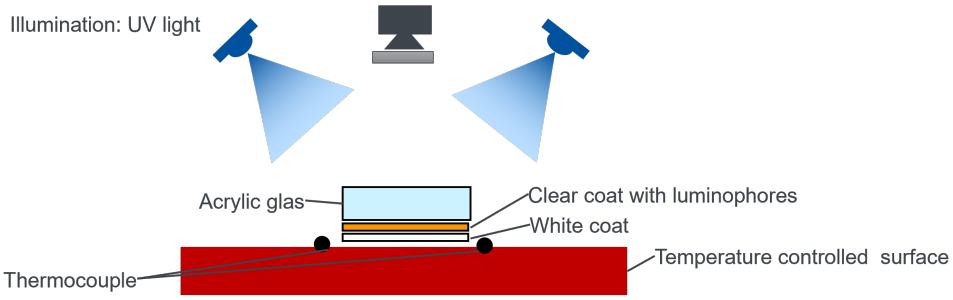



**Figure 4.** Schematic illustration of the TSP calibration setup.

Using the same camera system (camera, lens, and optical filter) and the same UV LEDs, the temperature-dependent TSP emission intensity was recorded. The distances and alignment of the camera and illumination system were similar to those in the main experiment. The sample was heated in 1 K increments from 22.3 °C to 59.0 °C, illuminated, and its emission recorded. The camera settings, including exposure time and aperture, were fixed and identical to those used in the main experiment. The sample temperature was determined from the mean of two thermocouples located on either side of the sample on the heated-plate surface. The calibration process was fully automated using LabVIEW and TestStand. Only images for which the plate temperature remained within $\pm 0.1$ K of the setpoint for five minutes were accepted. An ROI measuring 22 px $\times$ 76 px was defined in the centre of the frame (blue box in Figure 5), within which the TSP coating was assumed to be isothermal.

Ten images are captured for each valid calibration point. To reduce image noise, a mean image is calculated from these ten images (red boxes in Figure 5). This results in one averaged image per measured temperature. Dark images (DI) are generated in the same manner without illuminating the TSP. In total, 1672 pixels are evaluated within the ROI. Figure 6a shows the absolute intensity as a function of surface temperature for all pixels in the ROI; measurement points are connected only for visual clarity.

The pixel-wise absolute intensity curves exhibit a certain degree of variation. It is therefore assumed that the measured intensity $I(x, y, T)$ can be separated into a position-dependent factor $f(x, y)$, including illumination intensity, illumination angle, paint-layer thickness, and luminophore concentration, and a temperature-dependent factor $g(T)$.

$$I(x, y, T) = f(x, y)\, g(T) \tag{10}$$

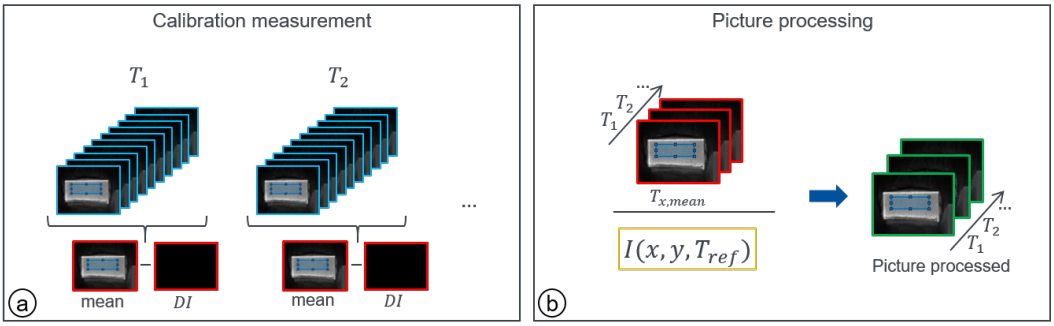
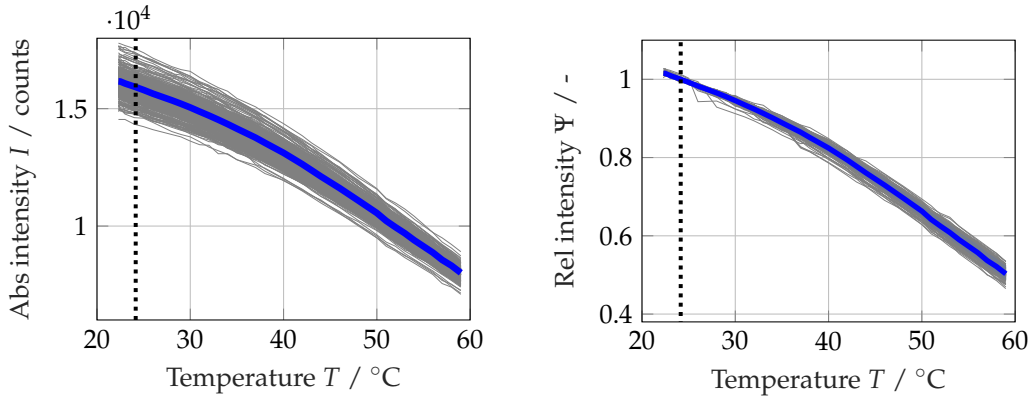



**Figure 5.** TSP calibration procedure: (**a**) definition of the region of interest (ROI) used to evaluate the calibration images; (**b**) image-processing workflow for calculating the intensity ratio from the averaged calibration image, the reference image, and the dark image (DI).




(**a**) (**b**)

**Figure 6.** Pixel-wise TSP calibration characteristics within the selected ROI: (**a**) absolute emission intensity as a function of temperature; (**b**) relative emission intensity after normalisation with the reference image. Grey lines represent individual pixel characteristics, the blue line indicates the ROI mean, and the black dotted vertical line marks the reference temperature.

Since the position-dependent parameters remain unchanged in both the experiment and the calibration, $f(x, y)$ remains constant for each pixel. By calculating a quotient $\Psi$ in which all measured intensities are normalised to a reference intensity at the reference temperature, $f(x, y)$ cancels out for the same spatial coordinates, and pixel-wise normalised temperature profiles can be analysed independently of local conditions.

$$\Psi = \frac{I(x, y, T)}{I(x, y, T_{\text{ref}})} = \frac{g(T)}{g(T_{\text{ref}})} \tag{11}$$

Figure 6b shows the resulting normalised profiles. Individual pixels are shown in grey, the ROI-averaged profile in blue, and the dotted line marks the reference temperature. The calibration reference temperature corresponds to the initial experimental temperature at $t = 0$ s. Each pixel-wise intensity profile is fitted with a fourth-order polynomial and evaluated at the reference temperature. This value provides the pixel-wise reference intensity. All temperature-dependent measurements are normalised according to Equation (11), and the calibration function is obtained from a further fourth-order polynomial fit.

After calibration, the inverse function converts intensity ratios into temperature. The function used here is shown in Figure 7, including the 95% interval determined from twice the standard deviation between the calibration function and the measurement points.

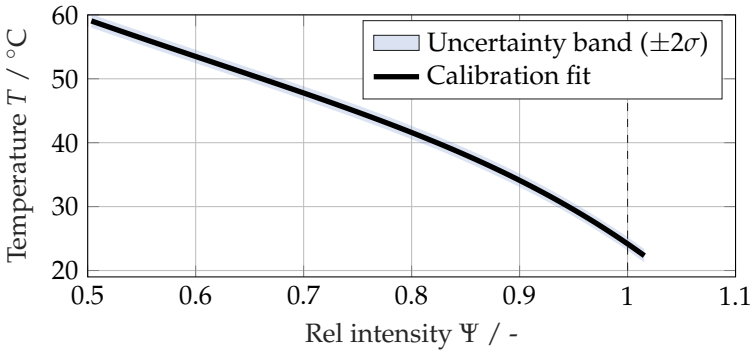



**Figure 7.** Inverse TSP calibration function used to convert the relative intensity ratio to temperature, including the 95% interval determined by twice the standard deviation from the calibration data.

It is modeled as

$$T(\Psi) = -130.033\Psi^4 + 251.9403\Psi^3 - 169.0882\Psi^2 - 13.6009\Psi + 84.9567 \quad (12)$$

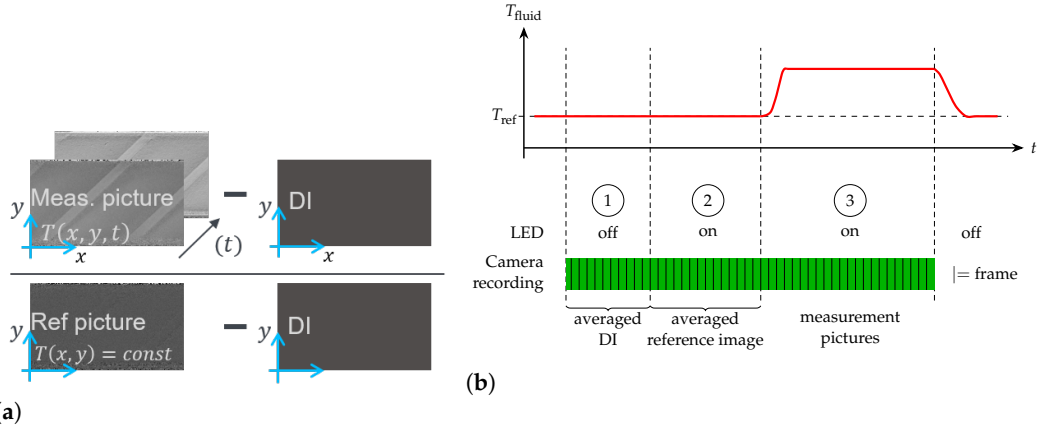
and valid only within the temperature range between 22.3 °C and 59.0 °C, with $R^2 = 0.99980$ and a 5th percentile of 0.99965. These values indicate a close relationship between $\Psi$ and $T$, confirm the homogeneity of the sample, and show that the geometric factor $f(x, y)$ is effectively eliminated. Due to the position correction, this function is used as a generally applicable calibration function throughout the entire field. Because the signal intensity decreases and its variance increases, the standard deviation rises from $\sigma_{\text{calibration,22.3 K}} = 0.3\,\text{K}$ to $\sigma_{\text{calibration,59.0 K}} = 0.6\,\text{K}$.

The aging of the TSP due to UV light was also investigated as part of the calibration measurement. At a plate temperature of 25 °C, we observed a decrease in intensity of 3% per hour of illumination. With a measurement time of 120 s, the aging of the TSP is neglected in the context of this study.

#### 4.3.3. TSP Post-Processing and Temperature Evaluation

During TSP post-processing, the measurement images are temporally and spatially cropped and then processed pixel by pixel, analogously to the calibration procedure. To eliminate local inhomogeneities, a quotient image is calculated by subtracting the unlit DI from each measurement image and dividing by the DI-corrected reference image (Figure 8a).

The reference image and DI are acquired immediately before each measurement. Both are averages of multiple frames: images 1–221 for the DI and images 222–521 for the reference image (Figure 8b). During DI acquisition, the UV LEDs are switched off and the TLC illumination is switched on to account for light-guiding effects from the TLC side of the PMMA. During reference-image acquisition, the sample is illuminated with UV light. Because of the long waiting time between experiments, the entire surface is assumed to be isothermal, and all visible structures are attributed to the position-dependent factor $f(x, y)$ in Equation (10). The reference temperature is measured using type-K thermocouples at the channel inlet and outlet. Using the measured initial temperature, $T_0 = T_{\text{ref}}$, the intensity ratio is converted into a temperature for every pixel and time step using the calibration curve in Figure 7 and Equation (12). The TSP technique therefore provides a temporally resolved temperature profile.




(**a**) (**b**)

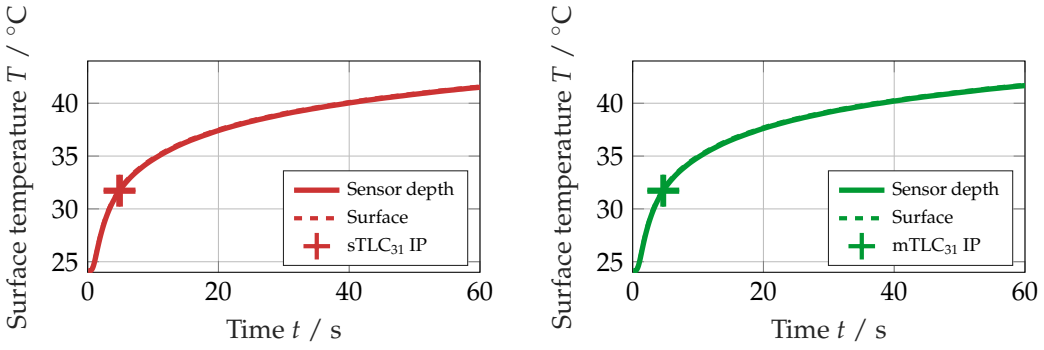
**Figure 8.** TSP measurement and post-processing procedure: (**a**) calculation of the quotient image; (**b**) acquisition sequence for the DI (Zone 1), reference image (Zone 2), and measurement images (Zone 3), together with the temporal fluid-temperature history $T_{\text{fluid}}$.

## 5. Results and Discussion

In this section, the HTCs of the three subchannels are determined and compared using four evaluations: $\text{sTLC}_{31}$, $\text{mTLC}_{31}$, $\text{mTLC}_{38}$, $\text{mTLC}_{31/38}$, and TSP. Because the established $\text{sTLC}_{31}$ measurement serves as the reference, all ratios are expressed relative to it. Temperature profiles measured with TSP at two representative locations are then examined, followed by a Monte Carlo uncertainty analysis.

### *5.1. Comparison of* $\text{sTLC}_{31}$ *and* $\text{mTLC}_{31}$

To verify that $\text{TLC}_{31}$ yields the same HTC distribution in the sTLC configuration (subchannel 3) and the mTLC configuration (subchannel 4), both $\text{TLC}_{31}$ layers are evaluated individually. The distance between the sensitive layer and the flow is equal in both subchannels (Figure 2). The SIW evaluation described in Section 2 requires an indication point (IP), consisting of an indication time and the corresponding temperature. Figure 9 illustrates the evaluation for the pixel at $(x, y) = (44, 17)$, hereafter denoted by $(44 \mid 17)$. This pixel is the example pixel used to perform the temperature profiles for all measurement probes, as well as the Monte Carlo simulation of the measurement uncertainty. The selection was made based on a pixel located in the middle range of the HTC for the geometry under investigation and subject to relatively simple flow patterns. The IP was recorded using $\text{sTLC}_{31}$ in Figure 9a and $\text{mTLC}_{31}$ in Figure 9b.




(**a**) $\text{sTLC}_{31}$. (**b**) $\text{mTLC}_{31}$.

**Figure 9.** Temporal surface-temperature evolution at pixel $(44 \mid 17)$ for the two $\text{TLC}_{31}$ configurations: (**a**) $\text{sTLC}_{31}$, yielding $h = 198.5\,\text{W m}^{-2}\,\text{K}^{-1}$; (**b**) $\text{mTLC}_{31}$, yielding $h = 206.4\,\text{W m}^{-2}\,\text{K}^{-1}$. The back-calculated temperature profiles and calibrated indication points are shown.

After synchronisation with the heater start time, the HTC is determined from the SIW equation. The corresponding analytical temperature histories at the channel surface and evaluation depth are shown in Figure 9. Applying the same analysis to every valid pixel yields the HTC maps in Figure 10, which use identical colour scales.

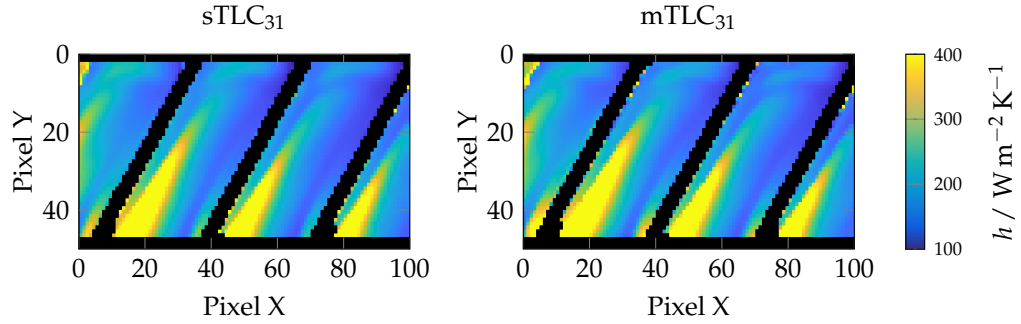



**Figure 10.** Comparison of the HTC distributions obtained with $sTLC_{31}$ in subchannel 3 and $mTLC_{31}$ in subchannel 4.

Both HTC maps show the same characteristic pattern. The ribs and channel walls are masked and appear as black regions. A low-HTC recirculation region is located directly downstream of each rib, followed by a slightly displaced high-HTC region and another region of lower heat transfer. The HTC in the upper part of the ROI (pixel rows 0–20) is lower than that farther below, and the peak HTC decreases from rib to rib in the streamwise direction. The results are therefore qualitatively consistent between the two subchannels and with the literature [15]. For a direct pixel-wise comparison, Figure 11 shows the mirrored axis distortion of fold change (MAD-FC) ratio proposed by Corliss et al. [25]. Unlike a plain ratio map, where underestimation and overestimation are visually asymmetric, MAD-FC applies a logarithmic colour mapping while retaining axis labels in fold-change units, so that equal relative deviations appear symmetric regardless of direction. A ratio $h_{\mathrm{mTLC}_{31}}/h_{\mathrm{sTLC}_{31}} = 1$ indicates equal HTCs; the symmetric limits 0.59 and 1.70 correspond to a halving and a doubling of the HTC, respectively.

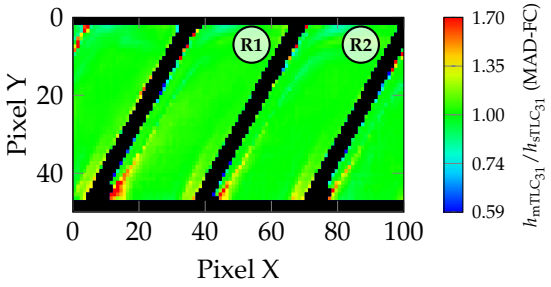



**Figure 11.** HTC distributions visualized with MAD-FC [25] obtained with $mTLC_{31}$ in subchannel 4 and $sTLC_{31}$ in subchannel 3. A ratio of one indicates equal HTCs; the scale is bounded by the symmetric multiplicative limits 0.59 and 1.70.

The MAD-FC map shows a high degree of agreement between the two measurements. Isolated deviations occur only in the lower corners, where high HTC values lead to short indication times and consequently greater measurement uncertainty.

All ratio statistics are evaluated in $\log_2$ space, consistent with the MAD-FC representation of the ratio maps. For a method $X$, the pixel-wise ratio field with respect to the common reference $sTLC_{31}$ is

$$\rho_{X,ij} = \frac{h_{X,ij}}{h_{\mathrm{sTLC}_{31},ij}}, \qquad (i,j) \in \Omega, \tag{13}$$

where $\Omega$ denotes one of the inter-rib regions $R1$ or $R2$ (Figure 11) and $N_\Omega$ the number of pixels for which all evaluations yield a valid HTC.

$$\widetilde{r}_{\mathrm{X/sTLC_{31}},\Omega} = 2^{\overline{\log_2 \rho_X}} = \left(\prod_{(i,j)\in\Omega} \rho_{X,ij}\right)^{1/N_\Omega} \tag{14}$$

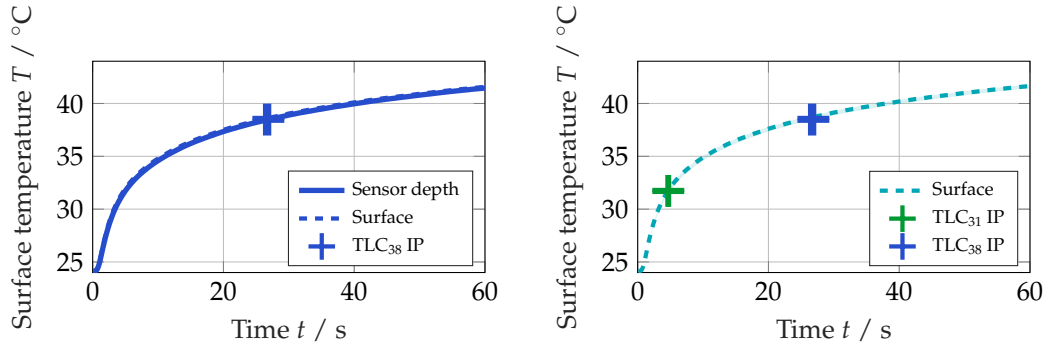
Instead of the arithmetic mean, the geometric mean $\widetilde{r}$ is used because it is invariant under inversion of the ratio, i.e., $\widetilde{r}(A/B) = 1/\widetilde{r}(B/A)$, so that the comparison does not depend on which technique appears in the denominator, and because it is the natural counterpart to logarithmic ratio mappings. Values of $\widetilde{r} = 1$ indicate identical HTC fields.

The deviation of the geometric mean of $\mathrm{mTLC_{31}}$ and $\mathrm{sTLC_{31}}$ is presented for both regions as a quotient below:

$$\widetilde{r}_{\mathrm{mTLC_{31}/sTLC_{31}},R1} = 1.041, \qquad \widetilde{r}_{\mathrm{mTLC_{31}/sTLC_{31}},R2} = 1.012.$$

### 5.2. *Comparison of* $\mathrm{sTLC_{31}}$ *and the* mTLC *Evaluations*

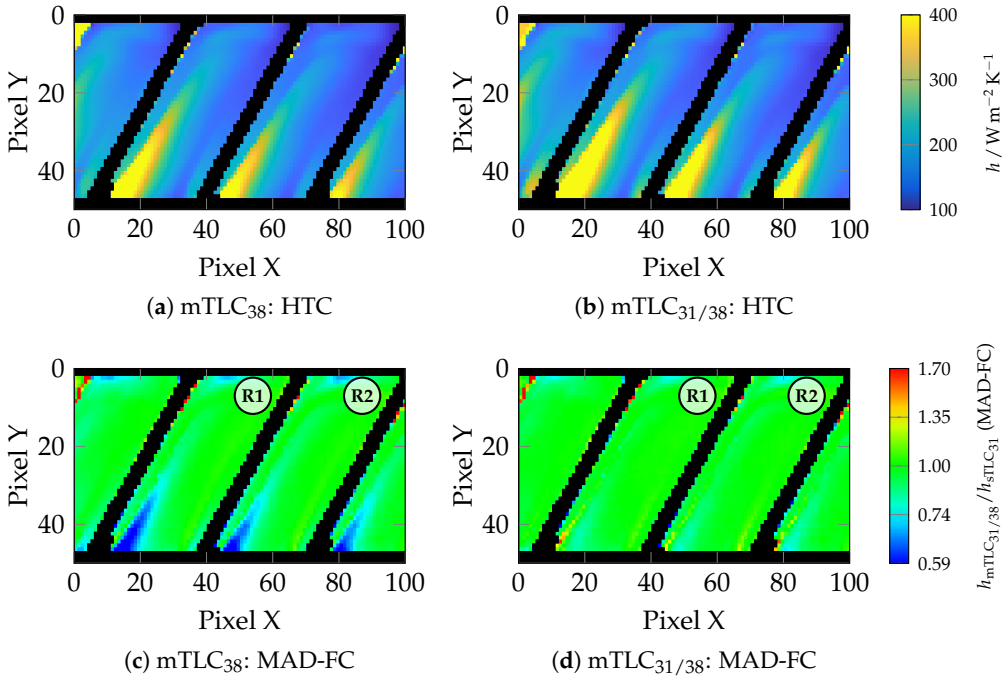
For the subsequent comparison, the mTLC configuration in subchannel 4 is analysed in full. Figure 12 shows the additional IP measured by the $\mathrm{mTLC_{38}}$ layer in blue. Both panels include the analytical surface-temperature history, equivalent to Figure 9a; Figure 12a additionally shows the analytical temperature at the sensor plane. All analyses use the representative pixel $(44 \mid 17)$. In Figure 12a, $\mathrm{mTLC_{38}}$ is evaluated individually by solving Equation (7) with one measurement point. The IPs in Figure 12b are identical to those in Figures 9b and 12a; using both points gives $M > 1$, and the HTC is determined according to Equation (8).




(**a**) $\mathrm{mTLC_{38}}$. (**b**) $\mathrm{mTLC_{31/38}}$.

**Figure 12.** Temporal surface-temperature evolution at pixel $(44 \mid 17)$ for the remaining mTLC evaluations: (**a**) $\mathrm{mTLC_{38}}$, yielding $h = 198.3\,\mathrm{W\,m^{-2}\,K^{-1}}$; (**b**) $\mathrm{mTLC_{31/38}}$, yielding $h = 202.1\,\mathrm{W\,m^{-2}\,K^{-1}}$. The indication points are $T_1 = 31.724\,^\circ\mathrm{C}$ at $t_1 = 4.68\,\mathrm{s}$ and $T_2 = 38.478\,^\circ\mathrm{C}$ at $t_2 = 26.87\,\mathrm{s}$. Both plots are limited to the first 60 s.

The HTC maps for $\mathrm{mTLC_{38}}$ and the combined $\mathrm{mTLC_{31/38}}$ evaluation are shown in Figures 13a and 13b, respectively. A direct comparison of the individually evaluated mTLC layers shows that the equally scaled high-HTC region obtained with $\mathrm{mTLC_{38}}$ is smaller and narrower than that obtained with $\mathrm{mTLC_{31}}$. This difference can be attributed to the greater relative timing uncertainty at short indication times in high-HTC regions. In lower-HTC regions, the indication times at both TLC temperatures are sufficiently long for this effect to become negligible. Nevertheless, $\mathrm{TLC_{31}}$ remains important because, for smaller temperature steps or thinner channel walls, $\mathrm{TLC_{38}}$ may not reach its indication temperature before the semi-infinite-wall assumption becomes invalid.




(**a**) $\mathrm{mTLC}_{38}$: HTC (**b**) $\mathrm{mTLC}_{31/38}$: HTC

(**c**) $\mathrm{mTLC}_{38}$: MAD-FC (**d**) $\mathrm{mTLC}_{31/38}$: MAD-FC

**Figure 13.** Comparison of the mTLC evaluations in subchannel 4: (**a**,**b**) HTC distributions obtained with $\mathrm{mTLC}_{38}$ and $\mathrm{mTLC}_{31/38}$; (**c**,**d**) corresponding MAD-FC [25] ratios relative to $\mathrm{sTLC}_{31}$ in subchannel 3. A ratio of one indicates identical HTCs; the MAD-FC scale is bounded by the symmetric multiplicative limits 0.59 and 1.70.

If both IPs are used, the high-HTC region expands slightly (Figure 13b). The corresponding MAD-FC maps in Figure 13c,d confirm this observation. In the high-HTC region, the values obtained with $\mathrm{mTLC}_{38}$ are significantly lower than those obtained with $\mathrm{sTLC}_{31}$. When both IPs are incorporated in the $\mathrm{mTLC}_{31/38}$ evaluation, this contrast remains visible but is less pronounced.

The geometric mean ratios are

$$\widetilde{r}_{\mathrm{mTLC}_{38}/\mathrm{sTLC}_{31},R1} = 0.922, \qquad \widetilde{r}_{\mathrm{mTLC}_{38}/\mathrm{sTLC}_{31},R2} = 0.932.$$

For the combined evaluation, they are

$$\widetilde{r}_{\mathrm{mTLC}_{31/38}/\mathrm{sTLC}_{31},R1} = 0.980, \qquad \widetilde{r}_{\mathrm{mTLC}_{31/38}/\mathrm{sTLC}_{31},R2} = 0.970.$$

### *5.3. Comparison of* $\mathrm{sTLC}_{31}$ *and* TSP

The HTC map obtained with $\mathrm{sTLC}_{31}$ is now compared with that obtained using TSP. The SIW method is again used; however, TSP provides one temperature value per pixel and frame. The evaluation described in Sections 2 and 5.2 is therefore extended to include all TSP support points. Figure 14 shows the resulting local HTC maps.

However, the TSP-based HTC map appears noisier and less uniform. The high-HTC region obtained with $\mathrm{sTLC}_{31}$ is aligned with the rib, and extends towards the lower channel wall. In the TSP result, this region is rounder but remains aligned with the rib, while a lower-HTC region appears near the lower channel wall. For the direct comparison, Figure 15a displays the MAD-based HTC-ratio map for TSP and $\mathrm{sTLC}_{31}$. Equation (14) yields geometric mean ratios of $\widetilde{r}_{\mathrm{TSP}/\mathrm{sTLC}_{31},R1} = 1.1278$ and $\widetilde{r}_{\mathrm{TSP}/\mathrm{sTLC}_{31},R2} = 1.1405$ for R1 and R2, corresponding to deviations of approximately 13% and 14%, respectively.

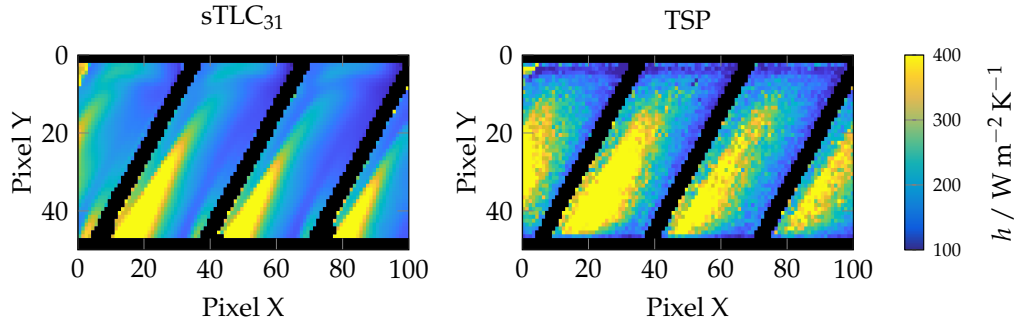
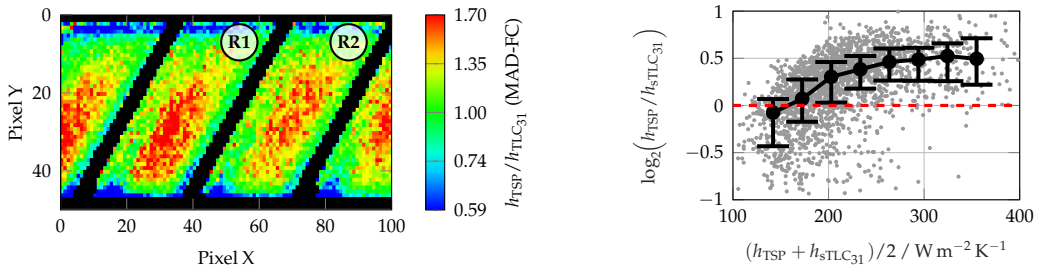



**Figure 14.** Comparison of the HTC distributions obtained with $sTLC_{31}$ in subchannel 3 and TSP in subchannel 2.



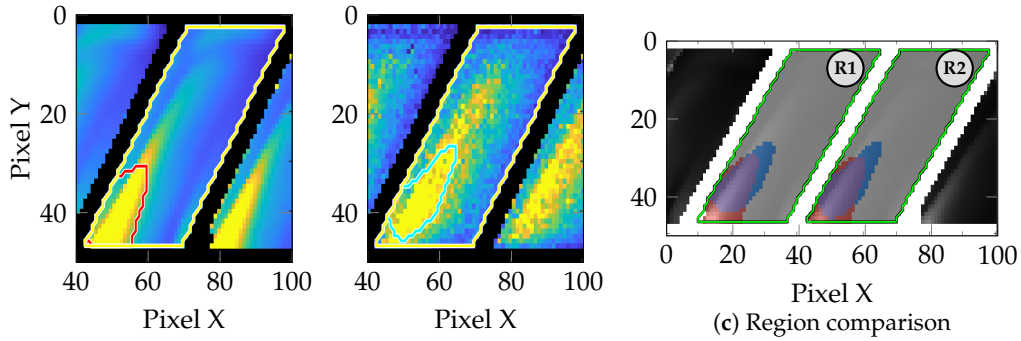

(**a**) MAD-FC comparison of the HTC distributions. (**b**) Bias versus mean HTC level.

**Figure 15.** Comparison of the HTC distributions obtained with TSP in subchannel 2 and $sTLC_{31}$ in subchannel 3: (**a**) MAD-FC comparison of the HTC distributions obtained with $sTLC_{31}$ in subchannel 3 and the TSP bounded by 1.70 and its reciprocal 0.59; (**b**) Bland-Altman-Plot for comparison of the mean HTC level for R1 and R2.

The MAD-FC map shows broad agreement between the techniques, with an O-shaped pattern in the peripheral regions. In the central region between two ribs, however, the HTCs determined by TSP are significantly larger than those obtained with $sTLC_{31}$; near the channel walls (approximately pixel rows 5 and 45), the opposite is observed. The logarithmic HTC deviation, based on the mean HTC of both techniques across all pixels in R1 and R2, is shown in Figure 15b. The data are divided into eight equidistant bins, represented by their means and standard deviations, together with a fitted trend. The divergence increases with increasing HTC. To investigate this behaviour in more detail, the area between two ribs is evaluated using the identical yellow parallelogram shown in Figure 16a,b. Within this mask, a contiguous high-HTC region is determined by regression analysis using an 85th-percentile threshold. This reveals the local displacement between the regions detected by $sTLC_{31}$ (red contour in Figure 16a) and TSP (cyan contour in Figure 16c). Figure 16 superimposes both detections and defines four regions: the full ROI, the common core, the TSP flank, and the sTLC flank.

This comparison shows that the high-HTC region detected by TSP is shifted towards the channel centre in both R1 and R2. The geometric mean HTC ratios for the four regions identified in Figure 16c are summarised in Table 4.

The table shows that the approximately 15% HTC deviation applies to the core, peripheral regions, and full ROI. Larger local deviations occur only at the two flanks. When both flanks are evaluated together, the two techniques again show reasonable agreement. To verify that these deviations do not result from an incorrect TSP-based HTC evaluation, the measured temperature histories are compared with the analytical predictions below.




(**a**) $sTLC_{31}$ (**b**) TSP (**c**) Region comparison

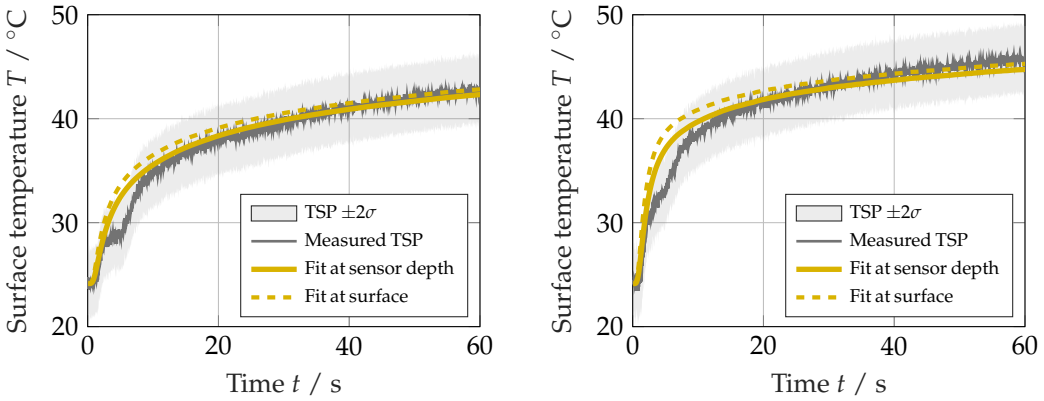
**Figure 16.** Definition and comparison of the high-gradient regions: (**a**) $sTLC_{31}$ and (**b**) TSP contour detections for pixel columns 40–100; (**c**) combined comparison over pixel columns 0–100, including regions R1 and R2.

**Table 4.** Geometric mean of the pixel-wise HTC ratio $h_{TSP}/h_{sTLC_{31}}$, calculated according to Equation (14) for the regions identified in Figure 16c.

| Region | Full ROI | Core | Flank TLC | Flank TSP | ROI Without Flanks and Core | Both Flanks |
|---|---|---|---|---|---|---|
| R1 | 1.1278 | 1.1548 | 0.6589 | 1.5695 | 1.1381 | 1.0169 |
| R2 | 1.1405 | 1.0444 | 0.7160 | 1.4055 | 1.1684 | 1.0032 |

### *5.4. Temporal Temperature Development*

One advantage of TSP is the availability of a complete temperature history. The SIW evaluation uses all temperature data collected during the measurement period. Figure 17a,b show measured TSP temperature histories at two locations within the ROI, together with the back-calculated analytical histories at the wall surface and TSP evaluation depth. Figure 17a represents a lower-HTC pixel ($h = 279.2\,W\,m^{-2}\,K^{-1}$), whereas Figure 17b represents a higher-HTC pixel ($h = 969.8\,W\,m^{-2}\,K^{-1}$).




(**a**) Pixel (44 | 17): $h = 279.2\,W\,m^{-2}\,K^{-1}$ and $R^2 = 0.964$. (**b**) Pixel (18 | 42): $h = 969.8\,W\,m^{-2}\,K^{-1}$ and $R^2 = 0.935$.

**Figure 17.** Temporal temperature evolution at two representative pixels within the evaluated region: (**a**) pixel (44 | 17); (**b**) pixel (18 | 42). The measured TSP temperatures are compared with the fitted temperature responses at the sensor-layer position and at the wall surface.

In low-HTC regions, the TSP temperature history exhibits a plateau at approximately 30 °C. Its duration depends on the HTC of the surrounding pixels; a smaller example is visible in Figure 17b. After the plateau, the measured trend again approaches the analytical

prediction. Heat conduction through the white coating alone is unlikely to explain this behaviour because the temperature initially rises immediately after the fluid-temperature increase. This can also be confirmed by analyzing the diffusion time of the coating layer, which, based on the condition $Fo = a\,t/\delta_{\mathrm{coat}}^2 = 1$, yields $t = \delta_{\mathrm{coat}}^2/a \approx 0.06\,\mathrm{s}$. The coating thus reaches thermal equilibrium within a single image, so that its thermal delay across its entire thickness is negligible. However, its thickness remains relevant for the evaluation depth $z$. Lateral heat conduction within the PMMA substrate is a more plausible cause of the plateau; if present, the resulting energy redistribution between regions of high and low heat input means that the one-dimensional assumption introduced in Section 2 holds only approximately in these regions. To estimate the order of magnitude of the lateral penetration length $L_{\mathrm{lat}}$, assuming a quasi-stationary process, it is derived from the fin parameter $m = \sqrt{h\,U/(k\,A_{\mathrm{c}})}$, whose reciprocal $L_{\mathrm{lat}} = 1/m$ gives the length over which a surface temperature gradient decays laterally. For a thermally penetrated layer of depth $\delta_{\mathrm{pen}} = \sqrt{a\,t}$ that is heated on one side only, $U/A_{\mathrm{c}} = 1/\delta_{\mathrm{pen}}$, so that

$$L_{\mathrm{lat}} = \sqrt{\frac{k\,\delta_{\mathrm{pen}}}{h}}. \tag{15}$$

In the case of high heat transfer at $h = 969.8\,\mathrm{W\,m^{-2}\,K^{-1}}$, the lateral penetration length amounts to approximately 0.6 px in the equally transformed pixel region of both measurement techniques after 10 s and increases to 1.0 px after 60 s. The longer the experiment lasts, the deeper the energy penetrates into the PMMA, and the more lateral heat conduction can occur. For $h = 279.2\,\mathrm{W\,m^{-2}\,K^{-1}}$, the lateral penetration length is approximately 1.2 px after 10 s and approximately 1.9 px after 60 s. Here, the influence of lateral heat conduction increases, since the convective input ($h$) becomes smaller while the lateral conduction ($k$) remains unchanged, which is why the lateral penetration length increases. Since the TLC evaluations rely on a single early indication ($t_{\mathrm{ind}} \approx 5\,\mathrm{s}$ for $\mathrm{TLC}_{31}$), whereas the TSP evaluation uses the entire recorded history, the two techniques are affected to a different extent by this time-dependent smearing. The resulting difference in length scale is comparable to the offset between the TLC and TSP contours in Figure 16c. This example is intended to provide a rough plausibility check and is not a rigorous study.

The complete TSP temperature history could support an evaluation model that explicitly accounts for lateral conduction; nevertheless, the same SIW method is retained here to ensure direct comparability between the techniques. The uncertainty bands shown in the curves represent a 95% interval based on the maximum calibration standard deviation in Figure 7, $\sigma_{\mathrm{calibration,59.0\,K}} = 0.6\,\mathrm{K}$, and an additional stability uncertainty of $\sigma_{\mathrm{add}} = 1\,\mathrm{K}$. The latter is obtained from the standard deviation of all pixels over 300 frames at constant temperature. A conservative combined value of $\sigma = 1.643\,\mathrm{K}$ is used. Its influence on the HTC is examined for the representative pixel $(44 \mid 17)$.

### *5.5. Monte Carlo Uncertainty Analysis*

The HTC uncertainty was propagated using Monte Carlo simulations according to Forster et al. [26]. The standard uncertainties assigned to the TLC and TSP input quantities are summarised in Table 5 and applied to the representative pixel $(44 \mid 17)$. All input quantities with nonzero uncertainty are modelled using normal distributions, except for the synchronisation offset, which follows a rectangular distribution, and the indication time, which follows an asymmetric distribution around its nominal value [26].

The resulting HTC distributions are summarised in Table 6. Central 95% intervals are reported directly because the propagated distributions are asymmetric.

The individually evaluated TLC configurations, $\mathrm{sTLC}_{31}$, $\mathrm{mTLC}_{31}$, and $\mathrm{mTLC}_{38}$, exhibit the widest 95% intervals for the representative pixel. The interval for $\mathrm{mTLC}_{38}$ is narrower

than those for the $TLC_{31}$ evaluations because of its longer indication time. The combined $mTLC_{31/38}$ evaluation has the smallest relative interval, $[-4.61, +5.03]\%$, and is therefore the most precise approach in this comparison. Despite the substantially larger absolute temperature uncertainty of TSP, $\sigma_{T,\mathrm{TSP}} = 1.6\,\mathrm{K}$ compared with $\sigma_{T,\mathrm{TLC}} = 0.102\,\mathrm{K}$, the TSP-based HTC evaluation remains comparably stable. The variance contributions of the grouped input quantities are listed in Table 7.

**Table 5.** Input quantities and associated standard uncertainties used for the Monte Carlo propagation of the TLC and TSP evaluations. A dash indicates that the quantity is not applicable to the respective technique.

| Quantity | Unit | TLC Nominal | TLC $u(X)$ | TSP Nominal | TSP $u(X)$ |
|---|---|---|---|---|---|
| Thermal conductivity $k$ | $\mathrm{W\,m^{-1}\,K^{-1}}$ | 0.190 | 0.00194 | 0.190 | 0.00194 |
| Density $\rho$ | $\mathrm{kg\,m^{-3}}$ | 1190 | 1.214 | 1190 | 1.214 |
| Specific heat capacity $c_p$ | $\mathrm{J\,kg^{-1}\,K^{-1}}$ | 1470 | 37.501 | 1470 | 37.501 |
| $T_{\mathrm{ind},A}$ | °C | 31.724 | 0.102 | – | – |
| $z_A$ | µm | 13.055 | 5.000 | – | – |
| $T_{\mathrm{ind},B}$ | °C | 38.478 | 0.102 | – | – |
| $z_B$ | µm | 22.890 | 5.000 | – | – |
| $T_{\mathrm{ref}}$, time-resolved | K | 0 | 0.102 | – | – |
| $T_{\mathrm{ref}}$, ideal step | K | 0 | 0.102 | – | – |
| $T_{\mathrm{ref}}$, systematic | K | 0 | 0 | – | – |
| TSP-layer depth $z$ | µm | – | – | 78.920 | 5.000 |
| $T_{\mathrm{TSP}}$, random | K | – | – | 0 | 1.600 |
| $T_{\mathrm{TSP}}$, common | K | – | – | 0 | 0 |
| $T_{\mathrm{fluid}}$, time-resolved | K | – | – | 0 | 0.102 |
| $T_{\mathrm{fluid}}$, systematic | K | – | – | 0 | 0 |
| Synchronization offset $t_{\mathrm{sync}}$ | s | 0 | 0.0577 | 0 | 0.0577 |

**Table 6.** Monte Carlo results for the evaluated heat transfer coefficients. The mean deviation and relative interval limits are referenced to the result obtained from the nominal input quantities. For TLC and TSP simulations 100,000 trials are used.

| Configuration | Nominal $h$ ($\mathrm{W\,m^{-2}\,K^{-1}}$) | MC Mean $h$ ($\mathrm{W\,m^{-2}\,K^{-1}}$) | Mean Deviation (%) | $u(h)$ ($\mathrm{W\,m^{-2}\,K^{-1}}$) | $u(h)/h$ (%) | Central 95% Interval ($\mathrm{W\,m^{-2}\,K^{-1}}$) | Relative 95% Interval (%) |
|---|---|---|---|---|---|---|---|
| $sTLC_{31}$ | 198.480 | 198.486 | 0.003 | 7.065 | 3.56 | [185.169, 212.783] | [−6.71, +7.21] |
| $mTLC_{31}$ | 206.458 | 206.737 | 0.135 | 7.002 | 3.39 | [193.435, 220.865] | [−6.31, +6.98] |
| $mTLC_{38}$ | 198.260 | 198.220 | −0.020 | 5.429 | 2.74 | [187.794, 209.002] | [−5.28, +5.42] |
| $mTLC_{31/38}$ | 202.456 | 202.689 | 0.115 | 5.022 | 2.48 | [193.132, 212.635] | [−4.61, +5.03] |
| TSP | 265.663 | 265.807 | 0.054 | 7.687 | 2.89 | [251.189, 281.308] | [−5.45, +5.89] |

**Table 7.** Relative contributions of the grouped input quantities to the HTC variance. The TLC and TSP contributions were obtained from the one-at-a-time sensitivity analysis. Values are given in percent.

| Influence Group | $sTLC_{31}$ | $mTLC_{31}$ | $mTLC_{38}$ | $mTLC_{31/38}$ | TSP |
|---|---|---|---|---|---|
| Indication time $t_{\mathrm{ind}}$ | 26.3 | 15.7 | 7.6 | 10.7 | — |
| Measured temperature $T_{\mathrm{ind}}$ or $T_{\mathrm{TSP}}$ | 38.5 | 43.1 | 58.8 | 40.5 | 9.7 |
| Material properties $k$, $\rho$, and $c_p$ | 15.6 | 17.3 | 26.3 | 32.4 | 27.4 |
| Reference or fluid temperature | 0.5 | 0.6 | 0.7 | 0.5 | 53.2 |
| Synchronization offset $t_{\mathrm{sync}}$ | 10.0 | 12.5 | 0.4 | 8.3 | 1.1 |
| Sensitive-layer depth $z$ | 9.2 | 10.9 | 6.2 | 7.6 | 8.5 |

The dominant uncertainty sources vary between techniques. The indication time and indication temperature have the greatest influence on the $TLC_{31}$ evaluations, whereas the indication time is less influential for $mTLC_{38}$ and $mTLC_{31/38}$. For TSP, the fluid temperature and substrate properties are particularly important.

## 6. Conclusions

This study presents a simultaneous direct comparison of three wall-temperature measurement configurations applied in three geometrically identical ribbed subchannels: $sTLC_{31}$, mTLC containing $TLC_{31}$ and $TLC_{38}$, and TSP. The same transient SIW method is applied to all techniques to maximise comparability. First, $sTLC_{31}$ is compared with the individually evaluated $mTLC_{31}$ layer. Both configurations yield very similar HTC distributions, with geometric mean ratios differing by approximately 4% between the ribs. The subsequent comparison with $mTLC_{38}$ reveals a larger deviation of approximately 8%, primarily because short indication times increase the relative timing uncertainty. Combining both mTLC indication points in the $mTLC_{31/38}$ evaluation reduces the geometric mean deviation relative to $sTLC_{31}$ to approximately 2%.

The TSP measurements provide a continuous temperature history for every pixel but have a larger absolute temperature uncertainty. Their HTC maps differ systematically from the $sTLC_{31}$ reference, with geometric mean deviations of approximately 13%. The observed redistribution of the high-HTC region and the temperature plateau in low-HTC regions indicate lateral heat conduction within the substrate is discussed as a possible cause. Finally, the Monte Carlo analysis shows that $mTLC_{31/38}$ provides the smallest uncertainty for the representative pixel, followed by $mTLC_{38}$, TSP, $mTLC_{31}$ and $sTLC_{31}$.The dominant uncertainty sources differ substantially: the TLC evaluations are most sensitive to indication time and temperature, whereas the TSP evaluation is governed mainly by the fluid temperature and the substrate properties.

**Author Contributions:** Conceptualization, M.T.L., P.D.H., K.M. and R.P.; methodology, M.T.L. and P.D.H.; validation, M.T.L. and P.D.H.; formal analysis, M.T.L., P.D.H. and K.M.; investigation, M.T.L., P.D.H. and K.M.; writing—original draft preparation, M.T.L. and P.D.H.; writing—review and editing, R.P.; supervision, R.P.; project administration, R.P.; funding acquisition, R.P. All authors have read and agreed to the published version of the manuscript.

**Funding:** The work was supported by the Aviation Research Programme LuFo of the German Federal Ministry for Economic Affairs and Energy under project 20E2214, "Development and integration of a skin heat exchanger concept using a fibre-composite sandwich structure into the thermal management of electrified drive trains", and by the Bundesministerium für Wirtschaft und Energie (BMWE), following a resolution of the German Federal Parliament, under grant number 03EE5117G. The investigations were conducted as part of the joint research programme DigITecT within AG Turbo. The authors gratefully acknowledge AG Turbo and MTU Aero Engines AG for their support. The responsibility for the content lies solely with the authors.

**Institutional Review Board Statement:** Not applicable.

**Informed Consent Statement:** Not applicable.

**Data Availability Statement:** Data will be made available upon request.

**Conflicts of Interest:** The authors declare no conflicts of interest. The funders had no role in the design of the study; in the collection, analyses, or interpretation of data; in the writing of the manuscript; or in the decision to publish the results.

## Abbreviations

The following abbreviations are used in this manuscript:

| | |
|---|---|
| DI | Dark image |
| IP | Indication point |
| IRT | Infrared thermography |
| MAD-FC | Mirrored axis distortion of fold change |
| mTLC | Multi layer thermochromic liquid crystal |

| | |
|---|---|
| PMMA | Poly(methyl methacrylate) |
| SIW | Semi infinite wall method |
| sTLC | Single layer thermochromic liquid crystal |
| TLC | Thermochromic liquid crystal |
| TSP | Temperature sensitive paint |

## References


1. Kakade, V.; Lock, G.; Wilson, M.; Owen, J.; Mayhew, J. Accurate heat transfer measurements using thermochromic liquid crystal. Part 1: Calibration and characteristics of crystals. *Int. J. Heat Fluid Flow* **2009**, *30*, 939–949. [CrossRef]
2. Stasiek, J.; Stasiek, A.; Jewartowski, M.; Collins, M. Liquid crystal thermography and true-colour digital image processing. *Opt. Laser Technol.* **2006**, *38*, 243–256. [CrossRef]
3. Piasecka, M.; Piasecki, A.; Maciejewska, B. Liquid Crystal Thermography and Infrared Thermography Application in Heat Transfer Research on Flow Boiling in Minichannels. *Energies* **2025**, *18*, 940. [CrossRef]
4. Larschow, M.T.; Thissen, S.; Gugliuzza, J.; Zistler, S.; Carosella, S.; Middendorf, P.; Poser, R. Concept of Composite Folded Core Skin Heat Exchanger with Experimental Investigation of Surface Temperatures Using Temperature-Sensitive Paints. *Aerospace* **2026**, *13*, 246. [CrossRef]
5. Jeziorek, Ł.; Szafran, K.; Skalski, P. Heat Transfer Determined by the Temperature Sensitive Paint Method. *Trans. Aerosp. Res.* **2018**, *2018*, 45–57. [CrossRef]
6. Lee, J.J.; Dutton, J.C.; Jacobi, A.M. Application of temperature-sensitive paint for surface temperature measurement in heat transfer enhancement applications. *J. Mech. Sci. Technol.* **2007**, *21*, 1253–1262. [CrossRef]
7. Al Hashimi, H.; Hammer, C.F.; Lebon, M.T.; Zhang, D.; Kim, J. Phase-Change Heat Transfer Measurements Using Temperature-Sensitive Paints. *J. Heat Transf.* **2018**, *140*, 031601. [CrossRef]
8. Lorenz, M.; Horbach, T.; Schulz, A.; Bauer, H.J. A Novel Measuring Technique Utilizing Temperature Sensitive Paint—Measurement Procedure, Validation, Application, and Comparison With Infrared Thermography. *J. Turbomach.* **2013**, *135*, 031003. [CrossRef]
9. Vogel, G.; Weigand, B. A New Evaluation Method for Transient Liquid Crystal Experiments. In Proceedings of the ASME NHTC'01 35th National Heat Transfer Conference, Anaheim, CA, USA, 10–12 June 2001; Paper No. NHTC2001-20250.
10. Carslaw, H.S.; Jaeger, J.C. *Conduction of Heat in Solids*, 2nd ed.; Oxford Science Publications: Oxford, UK, 1959.
11. Von Wolfersdorf, J.; Hoecker, R.; Hirsch, C. A Data Reduction Procedure for Transient Heat Transfer Measurements in Long Internal Cooling Channels. *J. Heat Transf.* **1998**, *120*, 314–321. [CrossRef]
12. Duhamel, J.M.C. Mémoire sur la méthode générale relative au mouvement de la chaleur dans les corps solides plongés dans des milieux dont la température varie avec le temps. *J. L'ÉCole R. Polytech.* **1833**, *XIV*, 20–77.
13. Hägele, D.; Poser, R. A noise-resistant reformulation of duhamel's principle for discrete heat transfer evaluations. *SSRN Electron. J.* **2026**. [CrossRef]
14. Schulz, S.; Brack, S.; Terzis, A.; Von Wolfersdorf, J.; Ott, P. On the effects of coating thickness in transient heat transfer experiments using thermochromic liquid crystals. *Exp. Therm. Fluid Sci.* **2016**, *70*, 196–207. [CrossRef]
15. Krille, T.; Retzko, S.; Poser, R.; Von Wolfersdorf, J. Heat Transfer Measurements Using Multiple Thermochromic Liquid Crystals in Symmetric Cooling Channels. *J. Turbomach.* **2021**, *143*, 081005. [CrossRef]
16. Ireland, P.T.; Jones, T.V. Liquid crystal measurements of heat transfer and surface shear stress. *Meas. Sci. Technol.* **2000**, *11*, 969–986. [CrossRef]
17. LCR Hallcrest. *Technical Data Sheet—Sprayable TLC Coatings: SPN100 Series*; Technical Data Sheet TDS LC—SPN100; LCR Hallcrest: Glenview, IL, USA, 2023.
18. Poser, R.; Von Wolfersdorf, J. Transient Liquid Crystal Thermography in Complex Internal Cooling Systems. VKI Lecture Series 2010-05, Internal Cooling in Turbomachinery. 2010. Available online: https://scholar.google.com/citations?view_op=view_citation&hl=de&user=Pn5R4-oAAAAJ&cstart=20&pagesize=80&sortby=pubdate&citation_for_view=Pn5R4-oAAAAJ:blknAaTinKkC (accessed on 3 October 2026).
19. Poser, R.; Von Wolfersdorf, J. Liquid Crystal Thermography for Transient Heat Transfer Measurements in Complex Internal Cooling Systems. *Heat Transf. Res.* **2011**, *42*, 181–197. [CrossRef]
20. Kodzwa, P.M.; Eaton, J.K. Angular effects on thermochromic liquid crystal thermography. *Exp. Fluids* **2007**, *43*, 929–937. [CrossRef]
21. Hägele, P.D.; Schefthaler, V.; Gutiérrez De Arcos, D.; Waidmann, C.; Poser, R. Advances in the Analysis of Transient Heat Transfer Experiments Using Multiple Thermochromic Liquid Crystals. *Int. J. Heat Mass Transf.* **2026**, *271*, 129455. [CrossRef]
22. Banach, S. Sur les opérations dans les ensembles abstraits et leur application aux équations intégrales. *Fundam. Math.* **1922**, *3*, 133–181. [CrossRef]

23. Stoer, J.; Bulirsch, R. *Introduction to Numerical Analysis*, 3rd ed.; Number 12 in Texts in Applied Mathematics; Springer: Berlin/Heidelberg, Germany, 2002.
24. Liu, T.; Sullivan, J.P.; Asai, K.; Klein, C.; Egami, Y. *Pressure and Temperature Sensitive Paints*; Experimental Fluid Mechanics; Springer International Publishing: Berlin/Heidelberg, Germany, 2021. [CrossRef]
25. Corliss, B.A.; Wang, Y.; Driscoll, F.P.; Shakeri, H.; Bourne, P.E. MAD-FC: A fold change visualization with readability, proportionality, and symmetry. *PLoS ONE* **2024**, *19*, e0304632. [CrossRef]
26. Forster, M.; Seibold, F.; Krille, T.; Waidmann, C.; Weigand, B.; Poser, R. A Monte Carlo approach to evaluate the local measurement uncertainty in transient heat transfer experiments using liquid crystal thermography. *Measurement* **2022**, *190*, 110648. [CrossRef]

**Disclaimer/Publisher's Note:** The statements, opinions and data contained in all publications are solely those of the individual author(s) and contributor(s) and not of MDPI and/or the editor(s). MDPI and/or the editor(s) disclaim responsibility for any injury to people or property resulting from any ideas, methods, instructions or products referred to in the content.